ADVANCED SUSTAINABLE SYSTEMS
www.advsustainsys.com

Photoelectrochemical Hydrogen Production Using TiO_2/Mn-CdS Photoanode with ZnS Passivation and CoPi as Hole Transfer Relay

*Hwapyong Kim, Chaitanya B. Hiragond, Sung Wook Koo, Orim Lee, and Su-Il In**

To improve photoelectrochemical water splitting efficiency, it is crucial to simultaneously enhance light absorption, surface stability, and interfacial charge transfer. This work reports the rational design and fabrication of a multi-functional TiO_2/Mn-CdS/ZnS/CoPi photoanode that integrates these critical aspects. TiO_2 acts as a robust and conductive mesoporous film that absorbs UV light, while Mn-doped CdS broadens the absorption spectrum into the visible region owing to its narrower bandgap and suitable band alignment. To address the photocorrosion typically associated with CdS, a ZnS passivation is applied, offering chemical stability without impeding charge flow. Finally, cobalt phosphate is introduced as a surface catalyst to accelerate the oxygen evolution reaction, enhancing interfacial hole transfer and reducing the overpotential. This hierarchical architecture promotes synergistic interaction between each component, enabling efficient charge separation and transport. As a result, the TiO_2/Mn-CdS/ZnS/CoPi photoanode achieves an enhanced photocurrent density under illumination. These results highlight the effectiveness of integrating light-harvesting, protective, and catalytic components to achieve high-performance and stable operation in PEC water splitting.

1. Introduction

Photoelectrochemical (PEC) water splitting has emerged as a highly promising technology for the sustainable production of hydrogen, a clean and renewable energy carrier. Since the pioneering study by Honda and Fujishima, which first demonstrated PEC water splitting using TiO_2 nanocrystals, the field has witnessed extensive exploration and innovation.[1–4] Among various candidate materials, titanium dioxide (TiO_2) has firmly established itself as a cornerstone in PEC systems, owing to its widespread availability, low cost, and remarkable resistance to photocorrosion. These characteristics make TiO_2 particularly attractive as a photoanode material for water splitting in PEC applications.[5–12]

However, despite its numerous advantages, TiO_2 suffers from a significant limitation, namely relatively wide bandgap. The rutile phase of TiO_2 exhibits a bandgap of ≈3.0 eV, while the anatase phase has a slightly larger bandgap of ≈3.2 eV.[13–16] This restricts its ability to absorb sunlight efficiently, particularly in the visible region of the solar spectrum, thus constraining its overall photoresponse and solar-to-hydrogen (STH) conversion efficiency.

To overcome this challenge, many studies have proposed the development of heterostructures by integrating TiO_2 with narrower bandgap semiconductors. Such heterojunctions can significantly broaden the light absorption range and improve charge carrier dynamics, ultimately enhancing the PEC performance of TiO_2-based systems under visible light irradiation. In this context, cadmium sulfide (CdS) quantum dots (QDs) stand out as highly promising photosensitizers. CdS possesses a suitable bandgap of ≈2.4 eV, well aligned with the visible region of solar spectrum, and features conduction and valence band positions that are thermodynamically favorable for water splitting.[17–19]

Despite their potential, CdS-based photocatalysts face several practical challenges that limit their practical application. One of the most critical issues is photocorrosion, which deteriorates performacne and long-term stability. Photocorrosion is a critical issue wherein sulfur ions in CdS are attacked by photogenerated holes, resulting in their oxidation to elemental sulfur. This process leads to surface degradation and defect formation, and facilitates further redox reactions under aerobic conditions[20] and compromising the integrity and functionality of the CdS photoelectrode. Due to the photocorrosion problem of CdS, many studies have employed sacrificial agents, such as a combination of sodium sulfide (Na_2S) and sodium sulfite (Na_2SO_3) electrolyte, to achieve high photocurrent densities exceeding 4 mA cm^{-2}.[21–23]

H. Kim, C. B. Hiragond, S. W. Koo, O. Lee, S.-I. In
Department of Energy Science & Engineering
Daegu Gyeongbuk Institute of Science and Technology (DGIST)
Daegu 42988, Republic of Korea
E-mail: insuil@dgist.ac.kr

The ORCID identification number(s) for the author(s) of this article can be found under https://doi.org/10.1002/adsu.202500741

DOI: 10.1002/adsu.202500741

Na_2S and Na_2SO_3 act as hole scavengers in the electrolyte, donating electrons to the photogenerated holes that would otherwise oxidize the CdS lattice. However, the use of Na_2S/Na_2SO_3 poses several drawbacks, including the generation of environmentally harmful byproducts, limited long-term stability, and increased operational cost. For these reasons, the Na_2SO_4 electrolyte has been considered as an alternative for photoelectrochemical hydrogen production, although its performance remains relatively low.

Another key strategy explored in this research is the use of doping to modify the intrinsic properties of semiconducting nanocrystals. Doping with optically active transition metal ions, such as Mn^{2+}, has proven effective in tuning the electronic and photophysical properties of CdS nanocrystals.[24] The incorporation of Mn^{2+} introduces new electronic states within the midgap region of the sensitizer, thereby altering the charge separation and recombination dynamics in sensitized solar cells.[25] Additionally, Mn^{2+} ions can create shallow trap states, which extend the lifetime of charge carriers by scavenging photogenerated holes, thereby improving the overall efficiency of the photoelectrode.[26]

However, pure semiconductor nanoparticles such as CdS remain vulnerable to surface damage and environmental degradation. To mitigate these issues, surface modification of CdS nanocatalysts is essential, although such treatments may affecte their photocatalytic, chemical, and optical properties. This study proposes a surface passivation strategy using a ZnS shell layer, deposited via the successive ionic layer adsorption and reaction (SILAR) method. The ZnS layer protects the CdS core from photocorrosion, thereby enhancing its chemical stability and overall photocatalytic performance.

Moreover, in PEC water splitting, the sluggish kinetics of the oxygen evolution reaction (OER) at the anode represent a major bottleneck that limits the overall electrolytic efficiency. To address this challenge, the development of highly active and stable OER catalysts is essential. For decades, water oxidation catalysts (WOCs) have been in the spotlight for improving the PEC performance by reducing the electron and hole recombination rate.[27–31] The application of a WOCs can alter the reaction pathway of water oxidation and decrease the associated energy barrier, thereby accelerating the surface reaction kinetics. Among the various WOCs, cobalt phosphate (CoPi) has attracted considerable attention as a cocatalyst for coupling with photocatalysts, owing to its efficient performance, earth-abundant, and self-healing charateristics.[32–41] While the clear mechanism by which CoPi modification improves PEC performance remains under debate, a widely accepted explanation is that photo-induced holes oxidize Co ions to a higher valence state, which subsequently facilitates water oxidation before the Co ions return to their initial oxidation state.[42] Numerous semiconductor materials have been studied with the CoPi cocatalysts to take advantage of hole transfer acceleration.[43–49] Furthermore, CoPi exhibits stability and functionality across a broad pH range from 1 to 14.[50]

In this work, the PEC performance is further enhanced by depositing a CoPi OER catalyst onto the TiO_2/CdS/ZnS photoanode, which effectively improves the anode-side reaction kinetics and boosts the overall water splitting efficiency. In summary, this research contributes to the ongoing advances the field of PEC water splitting technologies by integrating several synergistic strategies—narrow-bandgap sensitization, transition metal ion doping, surface passivation, and catalytic enhancement. Through this multifaceted approach, the study aims to address key challenges in the field and pave the way for the development of efficient PEC systems for sustainable hydrogen production.

2. Results

2.1. Physicochemical and Optical Properties of TiO_2/Mn-CdS/ZnS/CoPi Photoanodes

2.1.1. Structure Characterization

X-ray diffraction (XRD) analysis was conducted to examine the changes in the crystalline structure of photocatalysts (Figure S1, Supporting Information). In the case of TiO_2/Mn-CdS/ZnS/CoPi, peaks were obserbved at 2θ values, 25.56° (101), 37.95° (004), 48.36° (200), 54.16° (105), 55.23° (221), 69.03° (116), and 75.5° (215) as consistent with previous reports (JCPDS Card No. 21-1272).[51] Moreover, the XRD pattern of CdS exhibited peaks 2θ values at 26.88 (002), 51.79 (112), 66.10 (203). According to a previous reported study, these XRD patterns indicate a structure of hexagonal phase CdS (JCPDS Card No. 96-101-1055).[52] The XRD diffraction peak observed at 2θ value of 33.50° (020) can be matched with cubic ZnS (JCPDS Card No. 96-500-0089). However, the main peaks 2θ values at 26.43° of CdS and at 28.91° of ZnS are difficult to distinguish, and distinct peaks for CdS, ZnS, and CoPi are not clearly observed in XRD patterns, likely due to the low concentration of CdS, ZnS, and CoPi.[53]

XPS studies were conducted to investigate the chemical composition of the TiO_2/Mn-CdS/ZnS/CoPi. In the fitted Ti 2p XPS spectrum of TiO_2/Mn-CdS/ZnS/CoPi, the peaks located at 464.00 and 458.20 eV are assigned to Ti $2p_{1/2}$ and Ti $2p_{3/2}$, respectively. (**Figure 1a**). The energy difference between these two peak's binding energy is approximately 5.8 eV, which is well assigned to Ti^{4+} state in the CdS-TiO_2 samples.[54,55] After coating Mn-CdS onto TiO_2 by SILAR process, Ti 2p peaks shifted to lower binding energies while Cd 3d peaks shifted to higher energy compared to the reported value of 404.75 eV for Cd $3d_{5/2}$ and 411.45 eV for Cd $3d_{3/2}$ (Figure S2, Supporting Information).[56] It suggests that electron transfer makes the change of surface electron density, facilitating the formation of a built-in electric field between TiO_2 and CdS and the establishment of heterojunction.[57] In addition, O 1s peaks are confirmed at 529.4, 530.8, and 532.9 eV (Figure 1b). The first peak of O 1s represents lattice oxygen of TiO_2.[58,59] The second and third peak of O1s are related to surface-adsorbed water species. It can be attributed to hydroxyl groups bonded to bridging oxygen sites ($O_{br}H$: 532.9 eV) or to Ti sites (Ti-OH: 532.9 eV).[60]

The Cd $3d_{5/2}$ and Cd $3d_{3/2}$ were observed at 411.80 and 405.13 eV, respectively, for TiO_2/Mn-CdS/ZnS/CoPi and were attributed to Cd^{2+} state of CdS. The gap between $3d_{5/2}$ and $3d_{3/2}$ is 6.67 eV approximately, which corresponds to the presence of the +2 Cd 3d at the surface on the TiO_2 (Figure 1c).[61] The splitting Zn 2p peaks of TiO_2/Mn-CdS/ZnS/CoPi indexed to Zn $2p_{1/2}$ and Zn $2p_{3/2}$ respectively, located at 1044.40 and 1021.38 eV, corresponding to Zn bonded to sulfur (Zn-S) (Figure 1d).[62] Furthermore, S 2p spectra of TiO_2/Mn-CdS/ZnS/CoPi exhibits a distinct peak at 159.29-163.24 eV (Figure 1e). The prominent S 2p peaks

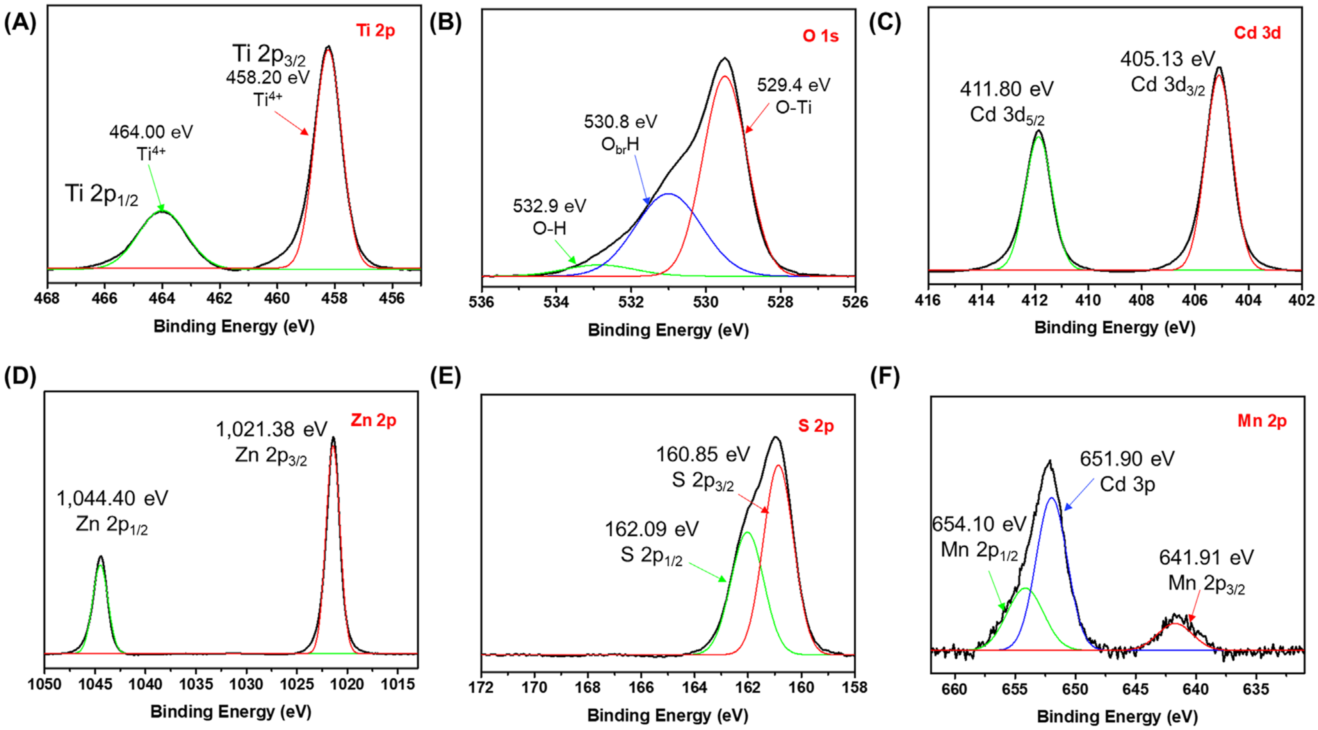

Figure 1. XPS analysis a) Ti, b) O, c) Cd, d) Zn, e) S, and f) Mn of TiO_2/Mn-CdS/ZnS/CoPi.

at 162.09 eV is the characteristic of the S^{2-} valence state.[63] To investigate the interaction of Mn-CdS and ZnS, the binding energy of Cd 3d and S 2p were compared before and after ZnS SILAR process (Figure S3, Supporting Information). After ZnS coating on TiO_2/Mn-CdS photoelectrode, the binding energies of Ti 2p are similar, while Cd 3d and S 2p shifted to higher energies. These results suggest that Cd of TiO_2/Mn-CdS could be partially substituted by Zn during ZnS SILAR process, indicating the formation of $Cd_{1-x}Zn_xS$ between CdS and ZnS.[64]

Mn 2p spectra indexed to Mn $2p_{1/2}$ and Mn $2p_{3/2}$ respectively, located at 654.10 and 641.91 eV (Figure 1f). Notably, the Mn $2p_{3/2}$ at 641.91 eV was attributed oxidation state of +2.[65] This indicatess that when Mn is doped into the CdS lattice, it can be detected by XPS at the corresponding binding energy, confirming that Mn predominantly exists in the +2 oxidation state.[66] Considering that Cd exists as Cd^{2+} in the CdS lattice, the substitution of Mn^{2+} at Cd^{2+} sites is the most plausible doping process. Introducing Mn into CdS causes the Cd 3d and S 2p XPS peaks to shift upward by 0.25 and 0.20 eV, respectively (Figure S4, Supporting Information). However, no peaks corresponding to Co were observed in the TiO_2/Mn-CdS/ZnS/CoPi samples due to the small amount of Co species. Furthermore, we can confirm the shielding effects of each coating layer. For example, the peak intensity of Ti 2p is suppressed after Mn-CdS SILAR process, and the peak intensity of CdS 3d diminishes after ZnS SILAR process. This shielding effect can effectively hinder the photogenerated electron transfer to the surface.[67]

Mn-doped cadmium sulfide (Mn-CdS) was deposited onto a mesoporous titanium dioxide (TiO_2) film to enhance the photoelectrochemical (PEC) performance of the resulting photoanode. The concentration of the Mn-CdS precursor solution was carefully optimized based on the photoelectrochemical characteristics, particularly the photocurrent density–voltage (*J*–*V*) plots (Figure S5, Supporting Information). Through this optimization, the optimal Mn-CdS loading condition (SILAR 4 cycles) was identified to maximize light absorption while maintaining efficient charge transport pathways within the photoanode structure.

The structural features of the fabricated TiO_2/Mn-CdS/ZnS/CoPi photoanode were investigated using field-emission scanning electron microscopy (FE-SEM), which provided cross-sectional images confirming total film thickness (**Figure 2**). To evaluate the spatial distribution and conformality of the CdS nanoparticles within the porous TiO_2 framework, energy-dispersive X-ray spectroscopy (EDS) analysis was conducted. The EDS elemental mapping confirmed a uniform distribution of Cd throughout the TiO_2 mesoporous film, indicating successful and homogeneous adsorption of the CdS sensitizer at each TiO_2 mesoporous film (Figure 2). Although the morphological difference between the TiO_2 film and the CdS particles was not clearly distinguishable under FE-SEM, compositional analysis revealed that CdS was predominantly deposited on the transparent TiO_2 film (TiO_2 (T)) rather than on the scattering TiO_2 film (TiO_2 (S)). This selective deposition is likely attributed to the difference in particle sizes between the two films; the smaller particles in the TiO_2 (T) film (particle size: 15–20 nm) provide a larger specific surface area than TiO_2 (S) film (particle size: >100 nm), facilitating higher CdS nanoparticle loading. The total thickness of the TiO_2/Mn-CdS/ZnS/CoPi photoanode was measured to be ≈7.48 µm (Figure 2). Further confirmation of well-dispersion was obtained through EDS mapping of Cd, Zn, S, and Co, which

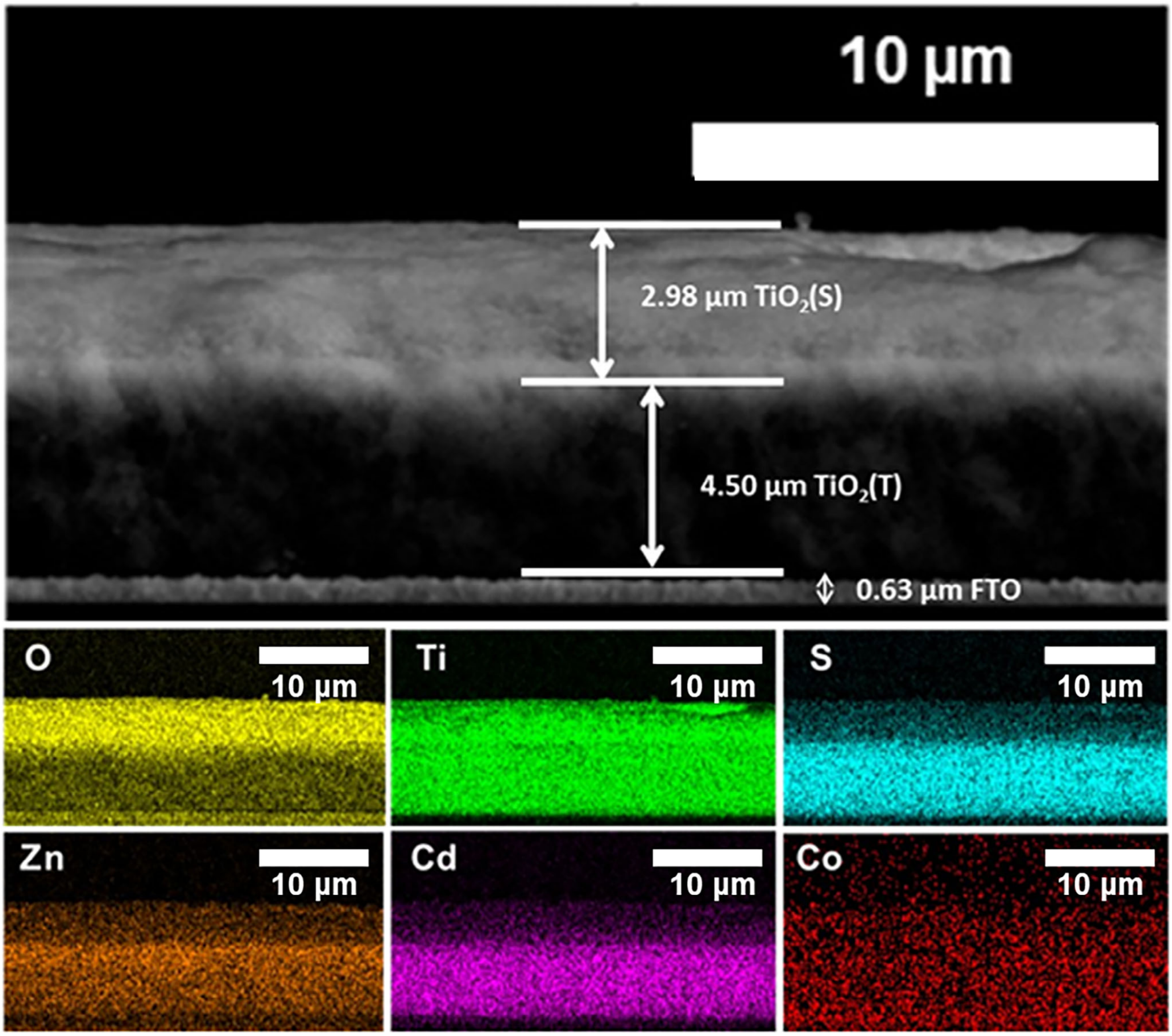

Figure 2. Cross-sectional SEM image and EDS spectrum of each element (O, Ti, S, Zn, Cd, and Co) for TiO_2/Mn-CdS/ZnS/CoPi photoanode.

demonstrated elemental distribution across the entire surface of the TiO_2 film, supporting the conformal coverage of the Mn-doped CdS, ZnS, and CoPi in TiO_2 film (Figure S6, Supporting Information).

High-resolution transmission electron microscopy (HR-TEM) studies showed that CdS and ZnS are well distributed on TiO_2 anatase nanoparticles (**Figure** 3a). It can be confirmed that the (002) plane of CdS and (111) plane of ZnS were attached to the (101) plane of TiO_2 (Figure 3b). The lattice fringes of TiO_2, CdS, and ZnS samples were clearly distinguishable, (101) of TiO_2, (002) of CdS, and (111) of ZnS also appeared. The (101), (002), and (111) planes exhibited d-spacings were 0.352, 0.179, and 0.316 nm, respectively (Figure 3c,d). Furthermore, elemental mapping TiO_2/Mn-CdS/ZnS/CoPi reveals a random distribution of Co and Mn, indicating a non-uniform interfacial arrangement (Figure 3e–l).

2.1.2. Optical Characterization

The Mn-doped CdS (Mn-CdS) sensitized photoanode exhibited enhanced light absorption compared to the bare TiO_2 photoanode, indicating more effective utilization of visible light for photoelectrochemical applications (**Figure** 4a). This enhancement can be attributed to the narrow bandgap and strong visible-light absorption properties of Mn-CdS, which effectively extend the optical response of the TiO_2-based system beyond the UV region. The optical properties of the photoanodes were further examined by UV–vis absorption spectroscopy, and the corresponding Tauc plots were used to estimate the optical bandgaps (E_g) of the samples. All three photoanode configurations-TiO_2/Mn-CdS, TiO_2/Mn-CdS/ZnS, and TiO_2/Mn-CdS/ZnS/CoPi-demonstrated bandgap narrowing compared to bare TiO_2, with absorption edges clearly extending into the visible light region (≈550 nm).

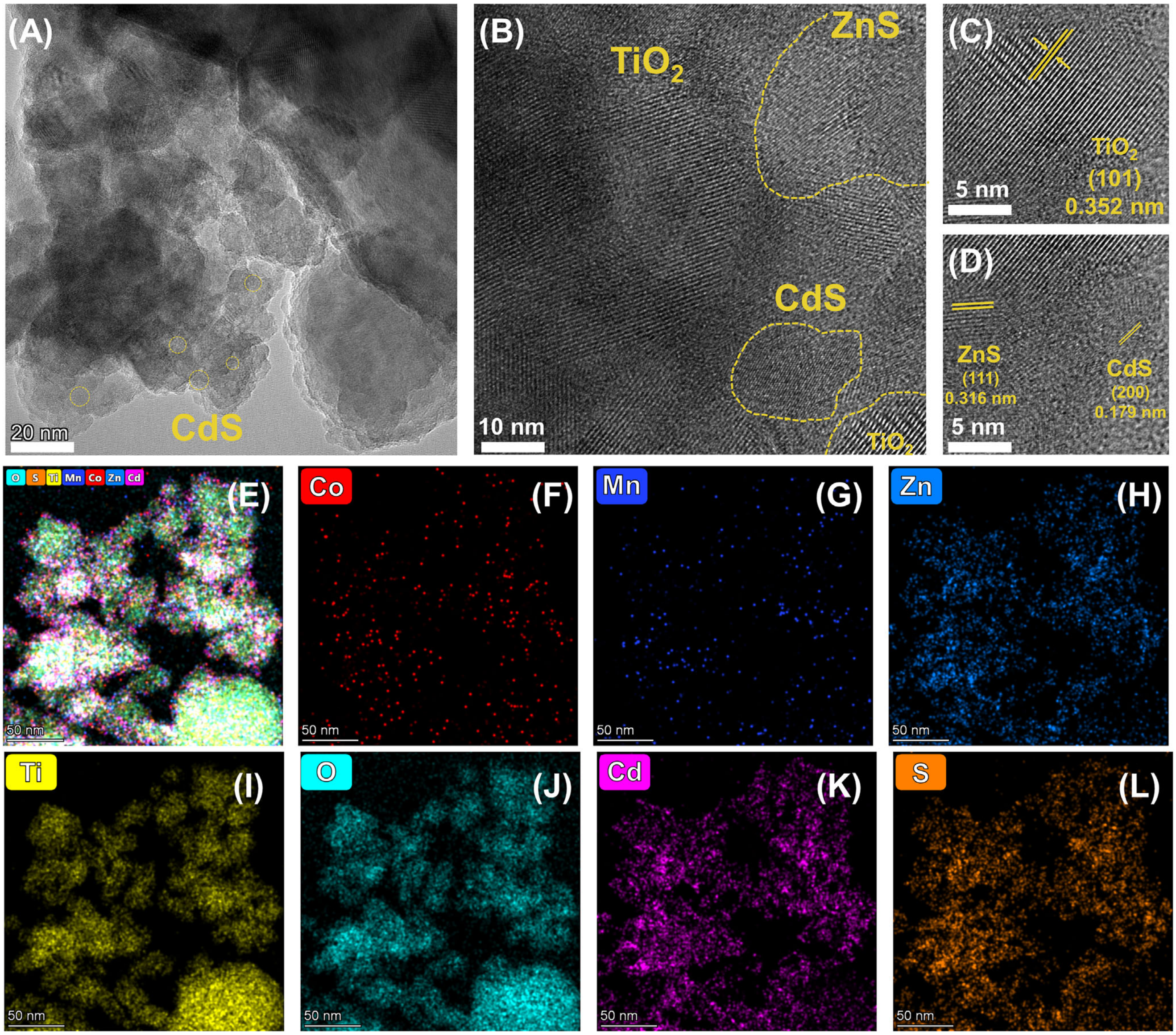

Figure 3. a) TEM and b) HR-TEM images of TiO_2/Mn-CdS/ZnS/CoPi and distinct d-spacing for c) TiO_2 and d) CdS and ZnS, respectively. e) Element mapping of Co, Mn, Zn, Ti.

Among them, the TiO_2/Mn-CdS/ZnS/CoPi photoanode showed an optical bandgap of ≈2.39 eV, as determined from the Tauc plot (Figure 4b). Furthermore, the bandgap of cubic ZnS is ≈3.6 eV, and it absorbs the light of wavelength below 340 nm.[68] TiO_2/Mn-CdS/ZnS photoanode exhibited a slight blue shift compared to TiO_2/Mn-CdS without ZnS, indicating a bandgap increase (≈ΔE_g: +0.03 eV). However, the light absorption of photoanode with CoPi was slightly lower than the photoanode without CoPi. These results reveal that CoPi interacts with CdS only at the surface via weak Co–S bonding and is not incorporated within the CdS crystal lattice. Therefore, CoPi covers the surface of photoanode and then blocks the light in the PEC even though it does not absorb light.[69,70]

In addition, the color of each component depends on light absorption properties. TiO_2 film exhibits white color thick film, but CdS and ZnS show different colors depending on thickness.[59] Bare TiO_2 and TiO_2/Mn-CdS films appeared white and brass-colored, respectively. This observation indicates that TiO_2, with its wide bandgap, does not absorb visible light, whereas CdS (>120 nm) absorbs photons with wavelengths shorter than ≈515 nm, leaving the yellow region unabsorbed and thereby imparting the characteristic yellowish (brass) color (Figure S7, Supporting Information). However, ZnS is too thin to exhibit a distinct chromatic color. Also, CoPi has bright purple color, but it was difficult to confirm a distinct color change after electrodeposition due to the low concentration of CoPi precursor.[72,73] To confirm the electrodeposition of CoPi, chronomaperometry measurements were carried out depending on the existence of $CoCl_2$ precursor (Figure S8, Supporting Information). In the absence of $CoCl_2$, the current density remained negligible, indicating that no

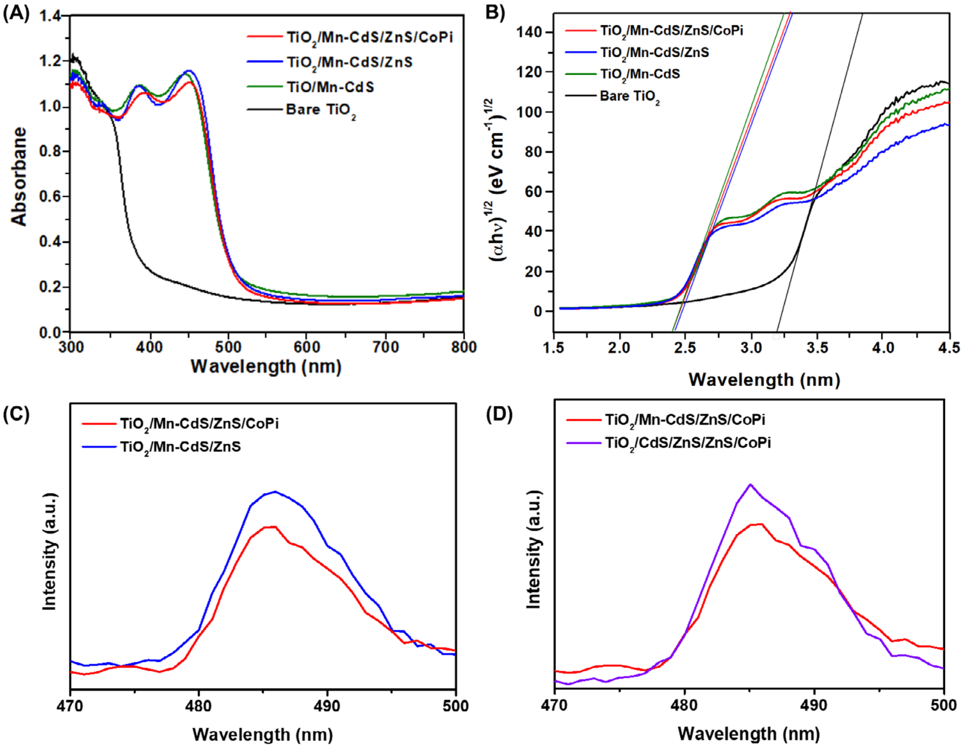

Figure 4. a) UV–vis Diffuse reflectance spectra and b) Tauc plot of Bare TiO_2, TiO_2/Mn-CdS, TiO_2/Mn-CdS/ZnS, and TiO_2/Mn-CdS/ZnS/CoPi samples. c) PL analysis of TiO_2/Mn-CdS/ZnS depended on CoPi and d) PL analysis of TiO_2/Mn-CdS/ZnS/CoPi depended on Mn doping.

deposition on the photoanode surface. In contrast, when $CoCl_2$ was added to the electrolyte, a distinct current density was detected, which can be attributed to the electrochemical deposition of CoPi.

Despite the additional deposition of ZnS and CoPi, the variation in the bandgap values among the three samples was not substantial. This is likely because the ZnS passivation and CoPi oxygen evolution reaction (OER) catalyst were deposited in relatively small quantities, insufficient to induce significant changes in the overall optical absorption characteristics of the photoanodes (Table S1, Supporting Information). These results collectively suggest that the enhanced light-harvesting capability of the photoanodes is primarily governed by the incorporation of Mn-CdS, which plays a dominant role in expanding the absorption range into the visible region, thereby improving the potential for solar energy conversion.

The photoluminescence (PL) intensity of the TiO_2/Mn-CdS/ZnS photoanode decreased after CoPi electrodeposition (Figure 4c). This quenching effect can be attributed to the extraction of photogenerated holes from the semiconductor to the CoPi sites, which suppresses radiative recombination. Furthermore, TiO_2/Mn-CdS/ZnS shows a strong band-edge exciton luminescence at 480 nm attributed to Mn doping (Figure 4d). Also, the PL intensity is slightly quenched after Mn^{2+} doping into CdS. Therefore, excitations are separated into electrons/holes effectively, and then electrons can move to the conduction band of TiO_2. Mn^{2+} dopant can minimize charge recombination.[71–73] The electron lifetime analysis was conducted by OCVD for TiO2-CdS with and without Mn doping (Figure S9, Supporting Information). The increase in electron lifetime upon Mn doping, together with the suppressed radiative recombination observed in the steady-state PL spectra, is consistent with prior studies reporting extended carrier lifetimes and improved charge separation in CdS-based structure.[74,75]

In other words, the reduction in PL intensity reflects accelerated charge separation at the interface, as holes are transferred from the valence band of Mn-CdS/ZnS to the CoPi cocatalyst. This enhanced hole transfer not only mitigates electron–hole recombination within the semiconductor but also promotes more efficient water oxidation at the surface, which is consistent with the improved photocurrent observed in PEC measurements.

Ultraviolet and X-ray photoelectron spectroscopy (UPS-XPS) measurements were carried out to determine band edge alignment of the photoanodes, providing insights into to thermodynamic barriers associated with water oxidation. The energy cutoff (E_C) edges were measured for Bare TiO_2 (16.47 eV), TiO_2/Mn-CdS (16.05 eV), TiO_2/Mn-CdS/ZnS (16.07 eV), TiO_2/Mn-CdS/ZnS/CoPi (16.18 eV), respectively. Furthermore, the valence band positions (EVB-XPS) for photoanodes were determined to be 2.40 eV (Bare TiO_2), 1.10 eV (TiO_2/Mn-CdS), 1.09 eV (TiO_2/Mn-CdS/ZnS), 1.07 eV (TiO_2/Mn-CdS/ZnS/CoPi) (Figure S10, Supporting Information). Bandgaps of photoanodes were calculated from tauc plots and used to determine the conduction band minimum for photoanodes. As shown in the schematic illustration of band alignments, it indicates that TiO_2/Mn-CdS/ZnS/CoPi is thermodynamically favorable for water oxidation reaction (Figure S11, Supporting Information). The band positions of TiO_2 and Mn–CdS are consistent with

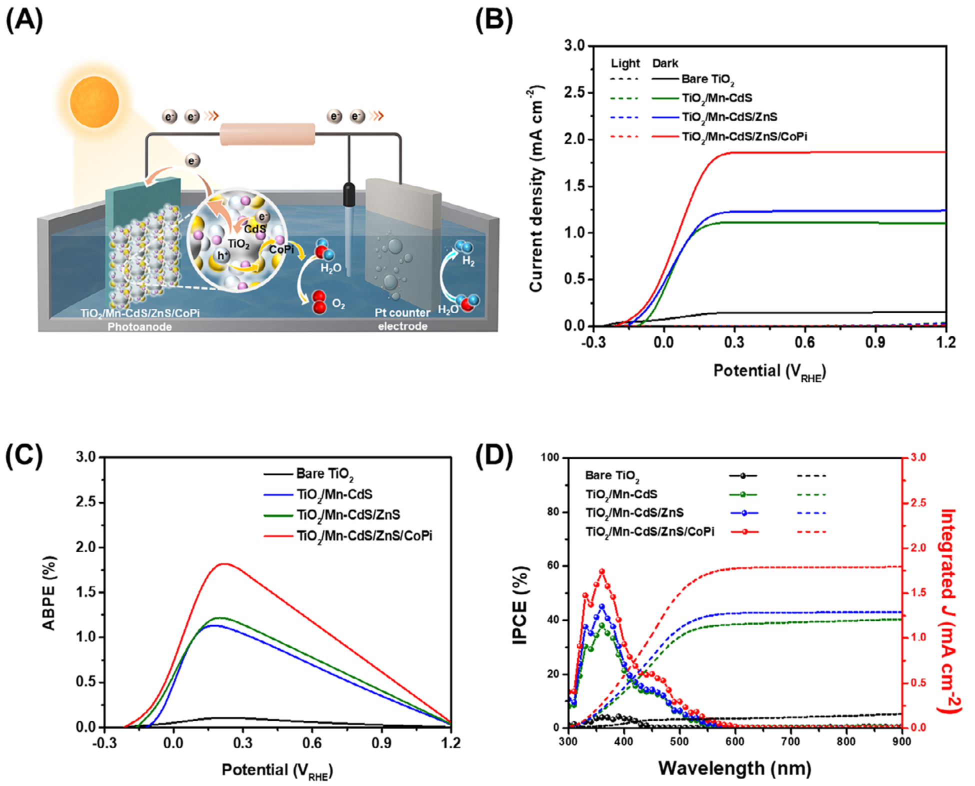

Figure 5. a) Schematic illustration of PEC using TiO_2/Mn-CdS/ZnS/CoPi photoanode. b) Photocurrent density and c) ABPE plots of Bare TiO_2, TiO_2/Mn-CdS, TiO_2/Mn-CdS/ZnS, and TiO_2/Mn-CdS/ZnS/CoPi photoanodes. d) IPCE spectra and integrated current density of photoanode samples.

previously reported values, indicating a favorable electronic coupling and energy-level alignment among the components, which supports the observed valence band shift in the XPS results. Recent studies have also reported similar interfacial electronic interactions in multicomponent photoanodes.[75] Furthermore, the valence band edge of TiO_2/Mn-CdS is higher than that of bare TiO_2, reflecting the electronic interaction between TiO_2 and Mn-CdS, as shown in Figure S10 (Supporting Information). This upward shift of the valence band, together with the corresponding conduction band alignment, modifies the overall band structure, which can explain the observed change in the visible appearance of the photoelectrode. These results highlight that the color change originates from the altered electronic structure. However, when comparing TiO_2/Mn-CdS with TiO_2/Mn-CdS/ZnS and TiO_2/Mn-CdS/ZnS/CoPi, the valence and conduction band positions remain largely unchanged, resulting in a similar visible appearance of the photoelectrodes.

2.1.3. Photoelectrochemical Analysis

The photocurrent density was systematically compared across different photoanode configurations prepared using varying precursor compositions, with measurements conducted under both light and dark conditions to evaluate their photoelectrochemical responses (**Figure** 5a,b). As detailed in Table S2 (Supporting Information), at an applied potential of 0.6 V_{RHE}, the measured photocurrent densities were 1.112 mA cm^{-2} for the TiO_2/Mn-CdS electrode, 1.233 mA cm^{-2} for the TiO_2/Mn-CdS/ZnS, and 1.863 mA cm^{-2} for the TiO_2/Mn-CdS/ZnS/CoPi photoanode. The highest current density observed for the photoanode coated with CoPi as hole transfer relay indicates a significant enhancement in catalytic performance due to the presence of CoPi, which acts as an efficient oxygen evolution reaction (OER) catalyst, facilitating hole extraction and improving interfacial charge transfer. This result underscores the importance of surface modification and catalytic engineering in improving PEC performance. The corresponding Applied Bias Photon-to-Current Efficiency (ABPE) curves, derived from the current density–voltage (*J*–*V*) characteristics, also reveal that the TiO_2/Mn-CdS/ZnS/CoPi electrode exhibits the highest ABPE among the tested samples (Figure 5c). Despite slight low light harvesting performance of TiO_2/Mn-CdS/ZnS/CoPi, TiO_2/Mn-CdS/ZnS/CoPi exhibited the highest incident photon-to-current efficiency (IPCE) among photoanode samples (Figure 5d). It indicates that CoPi facilitates interfacial charge transfer and thereby improves the photoelectrochemical response.

To investigate the effect of ZnS deposition on the photoelectrochemical performance, the number of ZnS deposited via successive ionic layer adsorption and reaction (SILAR) was controlled. The deposition cycles were adjusted to 1, 3, 5, and 7, and the corresponding photocurrent densities were measured. Among these, the sample with five ZnS SILAR cycles exhibited the highest photocurrent density of 1.13 mA cm^{-2}, indicating that an optimal amount of ZnS can significantly enhance the interfacial charge separation and transfer efficiency (Figure S12,

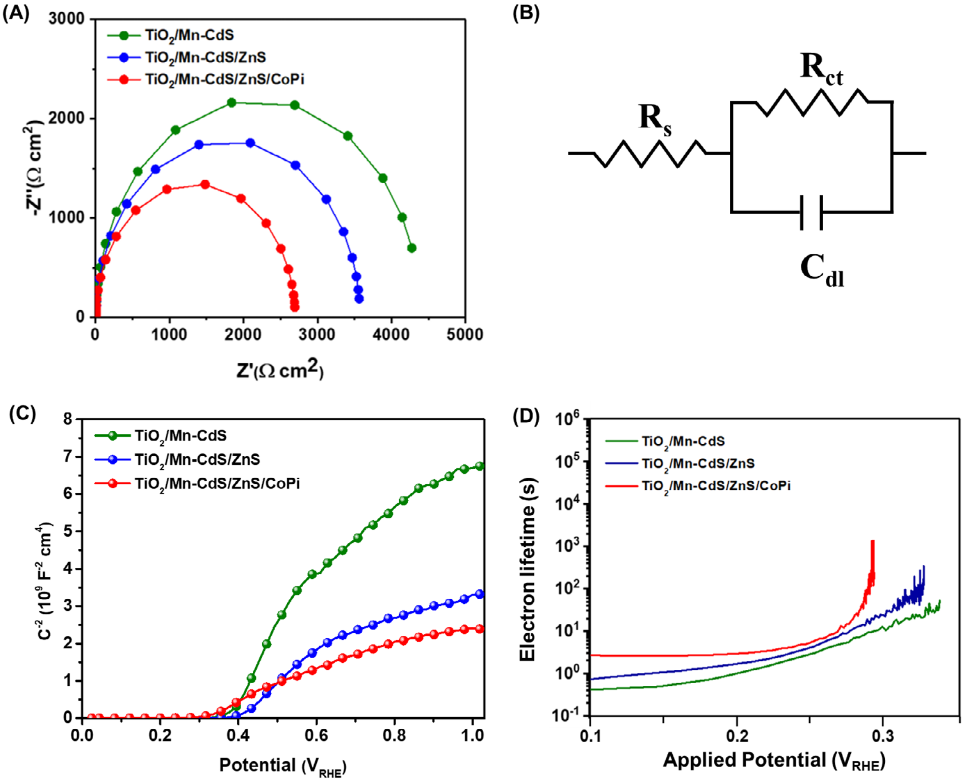

Figure 6. a) Nyquist plot, b) equivalent circuit, c) Mott-schottky plot, and d) electron lifetime of TiO_2/Mn-CdS, TiO_2/Mn-CdS/ZnS, and TiO_2/Mn-CdS/ZnS/CoPi photoanodes.

Supporting Information). In addition to the ZnS coating optimization, the CoPi catalyst was introduced via electrodeposition to further improve the photoanode performance. The electrodeposition duration was varied systematically, at 70, 110, 150, and 190 seconds, to determine the optimal CoPi loading. Among these, the sample treated for 150 seconds exhibited the highest photocurrent response, suggesting that this deposition time provides the most effective CoPi coverage without causing excessive recombination or blocking of active sites (Figure S13, Supporting Information).

To evaluate the durability of the photoanodes, daily *J*–*V* cycle tests were conducted by recording *J*–*V* plots every 24 h for 3 consecutive days (Figure S14, Supporting Information). After 3 days, the remaining photocurrent densities were 74%, 64%, 80%, and 79% for bare TiO_2, TiO_2/Mn-CdS, TiO_2/Mn-CdS/ZnS, and TiO_2/Mn-CdS/ZnS/CoPi, respectively. These results suggest that the incorporation of a ZnS passivation significantly improves the photostability of the Mn–CdS sensitized photoanode. In particular, the TiO_2/Mn-CdS/ZnS photoanode exhibited higher retention compared to TiO_2/Mn-CdS, indicating the protective role of ZnS.

To analyze the charge transfer and recombination of the fabricated photoanodes at the photoelectrode/electrolyte interface, electrochemical impedance spectroscopy (EIS) analysis was performed using TiO_2/Mn-CdS, TiO_2/Mn-CdS/ZnS, and TiO_2/Mn-CdS/ZnS/CoPi configurations. The R_s shows the series resistance of the photoelectrochemical device, such as solution resistance affected by electrolyte concentration. The R_s values of all photoanodes show similar value, indicating that other system resistance does not significantly influence to results (Table S3, Supporting Information).

The charge-transfer resistance (R_{ct}), derived from fitting the Nyquist plots to an equivalent RC circuit, reflects the charge-transfer kinetics at the photoanode–electrolyte interface (**Figure** 6a,b). Among the samples tested, the TiO_2/Mn-CdS/ZnS/CoPi photoanode exhibited the lowest R_{ct} value, indicating significantly improved charge transfer compared to the other photoanodes. The further decreased R_{ct} value of TiO_2/Mn-CdS/ZnS/CoPi photoanode suggests that the presence of CoPi creates more favorable physicochemical conditions for hole transfer from surface of photoanode to electrolyte, created by the CoPi site. As a result, water oxidation reaction at photoanode was easier to reduce the charge resistance barrier as reported.[39] Therefore, the CoPi introduced onto the surface is reasonably identified as a hole transfer accelerator at the photoelectrode/electrolyte interface, enabling fast surface chemical reaction.

To evaluate the flat-band potential (V_{FB}) and carrier concentration of each photoanode, Mott-Schottky (M-S) analysis was performed (Figure 6c). All photoanodes exhibited MM-S plots with a positive slope, consistent with n-type properties of TiO_2 and CdS semiconductor. The donor concentration (N_d) and V_{FB} are listed in Table S4 (Supporting Information). TiO_2/Mn-CdS/ZnS/CoPi photoanode exhibits the most negative V_{FB} and the highest N_d among four photoanodes, which is attributed to more efficient charge separation and photogenerated charge transfer compared to other photoanodes. These results can be attributed to reduced electron recombination at the interface of electrolyte and nonradiative recombination for TiO_2/Mn-CdS/ZnS/CoPi photoanode.[14]

Further analysis of charge recombination dynamics was conducted using the open-circuit voltage decay (OCVD) method to evaluate the electron lifetime (τ_e) of each photoanode. In this approach, the photoanodes were illuminated under constant light intensity (100 mW cm^{-2}), followed by abrupt cessation of illumination while monitoring the decay of the open-circuit voltage (V_{oc}). The electron lifetime was calculated from the transient V_{oc} plots using the established relationship between τ_e and the rate of voltage decay. The TiO_2/Mn-CdS/ZnS/CoPi photoanode demonstrated the longest τ_e, suggesting suppressed electron-hole recombination and more efficient charge separation (Figure 6d). These findings confirm that the sequential introduction of ZnS and CoPi enhances the PEC performance. In particular, ZnS mainly serves to passivate surface defect states in CdS, thereby reducing non-radiative recombination and promoting more efficient charge separation. W CoPi further accelerates interfacial hole extraction, leading to improved overall photoelectrochemical reaction.

The hydrogen evolution performance of the fabricated photoanodes was systematically evaluated through chronoamperometric measurements conducted under continuous AM 1.5G illumination for 1 hour in a standard photoelectrochemical cells setup. A constant external bias of 0.6 V_{RHE} was applied during the measurements to drive the hydrogen evolution reaction (HER). Hydrogen gas produced at the counter electrode was collected in the headspace of the PEC reactor and subsequently quantified using gas chromatography (GC), enabling accurate determination of the evolved hydrogen volume. Three different photoanode configurations: TiO_2/Mn-CdS, TiO_2/Mn-CdS/ZnS, and TiO_2/Mn-CdS/ZnS/CoPi were tested. The amount of hydrogen evolved varied significantly depending on the surface modification applied to the base Mn-CdS sensitized photoanode. Among the three samples, the TiO_2/Mn-CdS/ZnS/CoPi photoanode achieved the highest hydrogen production, clearly outperforming the other two photoanodes (**Figure 7**). This superior performance can be attributed to the synergistic effects of the ZnS passivation and the CoPi OER catalyst. The ZnS plays a critical role in suppressing surface recombination by passivating trap states in the Mn-CdS and facilitating efficient charge transport.

To investigate the effect of the ZnS passivation on the stability of hydrogen evolution, the time-dependent hydrogen yield was compared for TiO_2/Mn-CdS photoanodes with and without ZnS. The TiO_2/Mn-CdS photoanode without the ZnS exhibited a rapid decline in hydrogen evolution rate, with the hydrogen yield reaching saturation after ≈30 minutes of illumination. In contrast, the TiO_2/Mn-CdS/ZnS photoanode, which incorporates the ZnS passivation, maintained a steady and continuous hydrogen generation rate throughout the entire 60-minute reaction. This observation indicates that the ZnS passivation effectively enhances the photochemical stability of the photoanode by suppressing surface recombination and protecting the underlying Mn-CdS from photocorrosion, thereby enabling sustained hydrogen production under prolonged illumination.

Meanwhile, the CoPi enhances the kinetics of the oxygen evolution reaction (OER), reducing the overpotential for OER and accelerating hole extraction from the photoanode surface. To evaluate the effect of the CoPi OER catalyst on the photoelectrochemical performance, time-dependent hydrogen generation was measured for TiO_2/Mn-CdS/ZnS photoanodes with and without CoPi modification. The incorporation of the CoPi significantly enhanced the catalytic reaction, resulting in approximately a fourfold increase in hydrogen yield compared to the photoanode without CoPi. This improvement highlights the critical role of CoPi in facilitating hole extraction and promoting water oxidation kinetics, thereby enhancing overall charge separation efficiency and catalytic activity during the PEC process. These combined effects significantly improve the spatial separation of photogenerated electron–hole pairs, making more electrons available for hydrogen evolution at the counter electrode. The incremental improvement in hydrogen evolution across the three photoanodes—from TiO_2/Mn-CdS to TiO_2/Mn-CdS/ZnS, and finally to TiO_2/Mn-CdS/ZnS/CoPi—demonstrates the effectiveness of each sequential surface modification step. These results confirm that both ZnS and CoPi contribute additively and synergistically to enhancing the overall photoelectrochemical performance of the TiO_2/Mn-CdS absorbed photoanode configuration under visible-light-driven conditions.

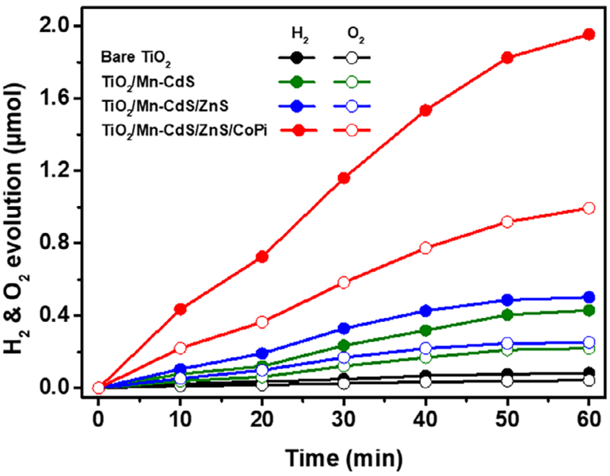

Figure 7. Hydrogen and oxygen yield over time measured at 0.6 V_{RHE} of photoanodes.

3. Conclusion

To achieve enhanced photoelectrochemical (PEC) efficiency, it is essential to simultaneously address multiple critical factors, including light absorption, surface passivation, and interfacial transfer. In this study, TiO_2/Mn-CdS/ZnS/CoPi photoanode was strategically designed and fabricated to synergistically incorporate these key functionalities. TiO_2 serves as a stable and conductive substrate that primarily absorbs ultraviolet light from the solar spectrum, while the Mn-doped CdS extends the light-harvesting capability into the visible region due to their narrower bandgap and favorable band alignment. To mitigate photocorrosion, which is a common issue for CdS-based materials under irradiation, a ZnS passivation was deposited as a passivation. Furthermore, the outermost deposition of cobalt phosphate serves as an oxygen evolution reaction (OER) catalyst, promoting efficient interfacial hole transfer from the photoanode to the electrolyte. The presence of CoPi enhances the kinetics of the anodic reaction, reducing the overpotential required for oxygen evolution and further contributing to overall performance improvements. As a result of this hierarchical and rational material design, the TiO_2/Mn-CdS/ZnS/CoPi photoanode demonstrated an enhanced photocurrent density of 1.863 mA cm^{-2} at 0.6 V_{RHE} and produced 1.96 µmol H_2 during 1 hour using 0.2 cm^{-2} surface area. Compared to other previous reported studies, ZnS passivation and CoPi combination for TiO_2/CdS exhibits superior performance in neural pH (≈pH 7.0) electrolyte (Table S5, Supporting Information). Overall, the performance enhancement is ascribed to the Co–Pi-mediated acceleration of hole transfer, supported by EIS and PL studies, and the increased durability is confirmed by *J*–*V* cycling tests.

These findings underscore the importance of combining light harvesting, surface protection, and catalytic enhancement strategies in a single architecture to achieve efficient and stable PEC water splitting.

4. Experimental Section

Mesoporous TiO_2 Photoanode Fabrication: Fluorine-doped Tin Oxide (FTO) glass (Pilkington, TEC-A7) was cleaned by sonification (15 min for acetone and ethanol) and UV/O_3 treatment (15 min). For the coating of a dense TiO_2 thin film onto the FTO glass, 7.5% solution of titanium diisopropoxide bis(acetylacetonate) in n-butanol was spin-casted, followed by annealing in the air (450 °C, 20 min). A commercial TiO_2 paste (Ti-Nanoxide T/SP, Solaronix, particle size: 15–20 nm) was further coated by the doctor blade technique and subsequently annealed in the air (500 °C, 30 min). A commercial TiO_2 paste (Ti-Nanoxide R/SP, Solaronix, particle size: $>$100 nm) was further coated by the doctor blade technique and subsequently annealed in the air (500 °C, 30 min).

CdS and ZnS Coating by Successive Ionic Layer Adsorption and Reaction (SILAR): SILAR deposition segregates the precursor reagents into two precursor solutions, the cation and anion dissolved in each respective solution. The substrate is then sequentially dipped into each precursor solution for a given period with subsequent rinsing. For CdS SILAR deposition from Cd^{2+} and S^{2-} precursors dissolved in ethanol, one SILAR cycle is typically defined as "metal cation precursor solution, rinse, anion precursor solution, rinse". Mn-CdS is deposited by 2–5 cycles.

During the first dip, Cd^{2+} adsorbs to the substrate surface. The solvent rinse removes unbound ions, and the second dip in S^{2-} facilitates the reaction with the surface-bound Cd^{2+} to yield CdS at Cd^{2+} adsorption sites. The rinsing step between successive precursor dips in the SILAR deposition scheme promotes heterogeneous growth because unbound ions are washed away, resulting in a semiconductor film in intimate contact with the substrate. ZnS are deposited by 1–7 cycles of a successive ionic layer adsorption and reaction (SILAR) process.

CoPi Catalyst Electrodeposit: For the synthesis, a three-electrode system was employed, comprising a 0.2 cm^2 working electrode, a Pt mesh counter electrode, and a saturated Ag/AgCl reference electrode. Cobalt(II) chloride hexahydrate served as the Co source, and a 0.1 м (pH 7) potassium phosphate buffer (KPi) was prepared by mixing ≈0.1 м NaH_2PO_4 and ≈0.1 м Na_2HPO_4, and 0.5 mм cobalt chloride hexahydrate. The electrodeposition was conducted at a voltage of 0.95 $V_{Ag/AgCl}$, with the measurement time varied to achieve CoPi with different thicknesses on the film.

Photoelectrochemical Performance Test: The PEC performance was evaluated in a quartz cell with a three-electrode system using a potentiostat. Working electrodes were used as photoanodes, and Pt mesh and Hg/HgO electrodes were used as counter electrodes and reference electrodes, respectively. The electrolyte for the PEC measurement was composed of 0.5 м sodium sulfate (Na_2SO_4) in deionized water (pH 7.0). Prior to measuring the *J*–*V* plots, dark current measurements were repeated five times to stabilize the photoanodes. Subsequently, the photoanodes were illuminated under 1 sun irradiation, and an external bias was applied using a potentiostat. From the *J*–*V* plots, ABPE was calculated according to where J_{ph} (mA cm^{-2}) is the measured photocurrent density, and V_{rev} is the standard-state reversible potential of water (1.23 V) using Equation (1). V_{app} (V) is the applied external potential versus RHE, and P_{in} is the power density of the incident light (100 mW cm^{-2}).

$$ABPE\ (\%) = \frac{J_{ph} \times (V_{rev} - V_{app})}{P_{in}} \tag{1}$$

Electrochemical impedance spectroscopy (EIS) analysis was carried out at 0.6 VRHE using potentiostat. A sinusoidal perturbation of ±10 mV with frequency range from 100 mHz to 1 kHz was applied for the nyquist plot analysis. M-S plot analysis was performed with an AC frequency 1 kHz and DC voltage from +1.02 V_{RHE} to 0.02 V_{RHE}. The incident photon-to-current efficiency (IPCE) was measured under an applied potential of 0.6 V_{RHE} and one-sun illumination using a 450 W solar simulator equipped with an AM 1.5 G filter and a monochromator (Cornerstone 130 1/8 m, Newport).

Mott–Schottky (M–S) measurements were performed in the potential range of +1.01 to 0.00 V_{RHE} under dark conditions at a frequency of 1 kHz. The donor density (N_d) and flat-band potential (V_{FB}) of the photoanodes were determined from the slope of the M–S plot and the extrapolated x-axis intercept, respectively. The electron lifetime (τ_e) value in each photoanode was evaluated using the open circuit voltage decay (OCVD) method. OCVD curves were obtained to measure the electron lifetime (τ_e) of the photoanode. The photoanode was irradiated by a constant light (100 mV cm^{-2}), which was suddenly switched off, and the photovoltage decay was then monitored. The τe values of the photoanode were calculated from the OCVD curves according to V based on the equation: Where V_{oc} (V) is the open-circuit voltage. The decay of open-circuit voltage (V_{OC}) caused by electron recombination at the photoanode-electrolyte interface after stationary illumination (1 sun condition) was suddenly switched off. The electron lifetime is calculated by Equation (2).

$$\tau_e\ (s) = \left(\frac{K_B T}{e}\right)\left(\frac{dV_{OC}}{dt}\right)^{-1} \tag{2}$$

Characterization: The absorption spectra of various samples are obtained using an ultraviolet-visible near-infrared (UV-Vis-NIR) spectrometer (Agilent Technologies, Santa Clara, CA, USA, Cary 5000). The photoluminescence (PL) spectra of the samples were recorded using a FluoroMax-4 spectrofluorometer (Horiba Scientific) with an excitation wavelength of 380 nm. X-ray photoelectron spectroscopy (XPS) measurements were performed on a Thermo VG K-alpha system using an Al Kα radiation source. The crystalline structures of the prepared samples were examined by ex situ X-ray diffraction (XRD) using a Rigaku MiniFlex-600 equipped with a HyPix-400 MF 2D hybrid pixel array detector (maximum power: 600 W, tube voltage: 40 kV). Field-emission transmission electron microscopy (FE-TEM) images were obtained with a Hitachi HF-3300 microscope (Japan) operated at an acceleration voltage of 300 kV.

Supporting Information

Supporting Information is available from the Wiley Online Library or from the author.

Acknowledgements

This work was supported by Ministry of Science and ICT and the National research foundation of Korea (NRF) (2021R1A2C2009459 and 1.250022)

Conflict of Interest

The authors declare no conflict of interest.

Data Availability Statement

The data that support the findings of this study are available from the corresponding author upon reasonable request.

Keywords

cadmium selenide, cobalt phosphate, hydrogen, passivation, photoelectrochemical cells

Received: June 1, 2025
Revised: October 19, 2025
Published online:

---

[1] A. Fujishima, K. Honda, *Nature* **1972**, *238*, 37, https://doi.org/10.1038/238037a0.
[2] H. Kim, A. Choe, S. B. Ha, G. M. Narejo, S. W. Koo, J. S. Han, W. Chung, J.-Y. Kim, J. Yang, S.-I. In, *ChemSusChem* **2022**, *16*, 202201925, https://doi.org/10.1002/cssc.202201925.
[3] H. Kim, J. W. Seo, W. Chung, G. M. Narejo, S. W. Koo, J. S. Han, J. Yang, J.-Y. Kim, S.-I. In, *ChemSusChem* **2023**, *16*, 202202017, https://doi.org/10.1002/cssc.202202017.
[4] H. C. Lee, H. Kim, K. Kim, K. Lee, W. Chung, S. B. Ha, M. Kim, E. Ahn, S. Li, S. Ji, G. Lee, H. Ma, S. J. Lim, H. Choi, J.-Y. Kim, H. Ahn, S.-I. In, J. Yang, *Adv. Sci.* **2025**, *12*, 00829, https://doi.org/10.1002/advs.202500829.
[5] X. Ruan, X. Cui, Y. Cui, X. Fan, Z. Li, T. Xie, K. Ba, G. Jia, H. Zhang, L. Zhang, W. Zhang, X. Zhao, J. Leng, S. Jin, D. J. Singh, W. Zheng, *Adv. Energy Mater.* **2022**, *12*, 2200298, https://doi.org/10.1002/aenm.202200298.
[6] Q. Pan, A. Li, Y. Zhang, Y. Yang, C. Cheng, *Adv. Sci.* **2019**, *7*, 1902235, https://doi.org/10.1002/advs.201902235.
[7] Y. Tao, Z. Ma, W. Wang, C. Zhang, L. Fu, Q. Zhu, Y. Li, G. Li, D. Zhang, *Adv. Funct. Mater.* **2023**, *33*, 2211169, https://doi.org/10.1002/adfm.202211169.
[8] Z. Li, C. Yao, Y. Yu, Z. Cai, X. Wang, *Adv. Mater.* **2014**, *26*, 2262, https://doi.org/10.1002/adma.201303369.
[9] C. Gao, T. Wei, Y. Zhang, X. Song, Y. Huan, H. Liu, M. Zhao, J. Yu, X. Chen, *Adv. Mater.* **2019**, *31*, 1806596, https://doi.org/10.1002/adma.201806596.
[10] E. Gong, S. Ali, C. B. Hiragond, H. S. Kim, N. S. Powar, D. Kim, H. Kim, S.-I. In, *Energy Environ. Sci.* **2022**, *15*, 880, https://doi.org/10.1039/D1EE02714J.
[11] S. Franz, H. Arab, G. L. Chiarello, M. Bestetti, E. Selli, *Adv. Energy Mater.* **2020**, *10*, 2000652, https://doi.org/10.1002/aenm.202000652.
[12] C.-Y. Lee, A. C. Taylor, S. Beirne, G. G. Wallace, *Adv. Energy Mater.* **2017**, *7*, 1701060, https://doi.org/10.1002/aenm.201701060.
[13] X. Li, Z. Zhang, L. Chen, Z. Liu, J. Cheng, W. Ni, E. Xie, B. Wang, *J. Power Sources* **2014**, *269*, 866, https://doi.org/10.1016/j.jpowsour.2014.07.060.
[14] S. Li, S.-M. Jung, W. Chung, J.-W. Seo, H. Kim, S. I. Park, H. C. Lee, J. S. Han, S. B. Ha, I. Y. Kim, S.-I. In, J.-Y. Kim, J. Yang, *Carbon Energy* **2023**, *5*, 384, https://doi.org/10.1002/cey2.384.
[15] B. O'Regan, M. Grätzel, *Nature* **1991**, *353*, 737, https://doi.org/10.1038/353737a0.
[16] M. J. Kenney, M. Gong, Y. Li, J. Z. Wu, J. Feng, M. Lanza, H. Dai, *Science* **2013**, *342*, 836, https://doi.org/10.1126/science.1241327.
[17] X. Yue, S. Yi, R. Wang, Z. Zhang, S. Qiu, *Sci. Rep.* **2016**, *6*, 2268, https://doi.org/10.1038/srep22268.
[18] Y. Xu, M. A. A. Schoonen, *Am. Mineral.* **2000**, *85*, 543, https://doi.org/10.2138/am-2000-0416.
[19] H. Lee, J. W. Yang, J. Tan, J. Park, S. G. Shim, Y. S. Park, J. Yun, K. Kim, H. W. Jang, J. Moon, *Adv. Sci.* **2021**, *8*, 2102458, https://doi.org/10.1002/advs.202102458.
[20] L. Cheng, Q. Xiang, Y. Liao, H. Zhang, *Energy Environ. Sci.* **2015**, *11*, 1362, https://doi.org/10.1039/C7EE03640J.
[21] P. Peng, J. Ren, S. Wang, J. Huang, L. Zou, P. Yang, X. Pang, M. Zhang, Y. Su, W. Luo, W. Tao, J. Xie, *Langmuir* **2024**, *40*, 19711, https://doi.org/10.1021/acs.langmuir.4c02426.
[22] Q. Dai, Y. Li, Z. Qiu, H. Tian, Y. Pu, X. Chen, B. Lv, J. Wei, W. Wang, *ACS Appl. Nano Mater.* **2024**, *7*, 17441, https://doi.org/10.1021/acsanm.4c02485.
[23] K. K. Patra, P. A. Bharad, V. Jain, C. S. Gopinath, *J. Mater. Chem. A* **2019**, *7*, 3179, https://doi.org/10.1039/C8TA11307F.
[24] P. K. Santra, P. V. Kamat, *J. Am. Chem. Soc.* **2012**, *134*, 2508, https://doi.org/10.1021/ja211224s.
[25] L. Yu, Z. Li, Y. Liu, F. Cheng, S. Sun, *Appl. Surf. Sci.* **2014**, *305*, 359, https://doi.org/10.1016/j.apsusc.2014.03.090.
[26] Y. R. Smith, R. Gakhar, A. Merwin, S. K. Mohanty, D. Chidambaram, M. Misra, *Electrochim. Acta* **2014**, *135*, 503, https://doi.org/10.1016/j.electacta.2014.05.005.
[27] A. M. Hilbrands, S. Zhang, C. Zhou, G. Melani, D. H. Wi, D. Lee, Z. Xi, A. R. Head, M. Liu, G. Galli, K.-S. Choi, *J. Am. Chem. Soc.* **2023**, *145*, 23639, https://doi.org/10.1021/jacs.3c07722.
[28] J. Yang, C. Deng, Y. Lei, M. Duan, Y. Yang, X. Chen, S. Yang, J. Li, H. Sheng, W. Shi, C. Chen, J. Zhao, *Angew. Chem.* **2025**, *137*, 202416340, https://doi.org/10.1002/ange.202416340.
[29] F. Zhao, T. Cheng, X. Lu, N. Ghorai, Y. Yang, Y. V. Geletii, D. G. Musaev, C. L. Hill, T. Lian, *J. Am. Chem. Soc.* **2024**, *146*, 14600, https://doi.org/10.1021/jacs.4c01441.
[30] T. Wang, K. Song, H. Liu, H. Li, Y. Zhang, W. Ren, R. Zhang, K. Li, F. He, Z. Qin, H. Hou, *Chem. Eng. J.* **2025**, *509*, 161333, https://doi.org/10.1016/j.cej.2025.161333.
[31] D. Xu, X. Gao, Z. Gui, Y. Duan, Y. Li, X. Meng, N. Gao, W. Shi, *Chem. Eng. J.* **2025**, *303*, 120965, https://doi.org/10.1016/j.ces.2024.120965.
[32] D. A. Lutterman, Y. Surendranath, D. G. Nocera, *J. Am. Chem. Soc.* **2009**, *131*, 3838, https://doi.org/10.1021/ja900023k.
[33] B. Kim, T. Kim, K. Lee, J. Li, *ChemElectroChem* **2020**, *7*, 3578, https://doi.org/10.1002/celc.202000734.
[34] S. Anantharaj, V. Aravindan, *Adv. Energy Mater.* **2019**, *10*, 1902666, https://doi.org/10.1002/aenm.201902666.
[35] P. W. Menezes, C. Panda, C. Walter, M. Schwarze, M. Driess, *Adv. Funct. Mater.* **2019**, *29*, 1808632, https://doi.org/10.1002/adfm.201808632.
[36] H. Kim, J. Park, I. Park, K. Jin, S. E. Jerng, S. H. Kim, K. T. Nam, K. Kang, *Nat. Commun.* **2015**, *6*, 8253, https://doi.org/10.1038/ncomms9253.
[37] J. Saha, S. Verma, R. Ball, C. Subramaniam, R. Murugavel, *Small* **2019**, *16*, 1903334, https://doi.org/10.1002/smll.201903334.
[38] Z. Song, K. Wang, Q. Sun, L. Zhang, J. Li, D. Li, P.-W. Sze, Y. Liang, X. Sun, X.-Z. Fu, J.-L. Luo, *Adv. Sci.* **2021**, *8*, 2100498, https://doi.org/10.1002/advs.202100498.
[39] S. Liu, I. Zaharieva, L. D'Amario, S. Mebs, P. Kubella, F. Yang, P. Beyer, M. Haumann, H. Dau, *Adv. Energy Mater.* **2022**, *12*, 2202914, https://doi.org/10.1002/aenm.202202914.
[40] L. Yang, H. Ren, Q. Liang, K. N. Dinh, R. Dangol, Q. Yan, *Small* **2020**, *16*, 1906766, https://doi.org/10.1002/smll.201906766.
[41] H. S. Ahn, T. D. Tilley, *Adv. Funct. Mater.* **2021**, *23*, 227, https://doi.org/10.1002/adfm.201200920.
[42] G. Ai, H. Li, S. Liu, R. Mo, J. Zhong, *Adv. Funct. Mater.* **2015**, *25*, 5706, https://doi.org/10.1002/adfm.201502461.
[43] M. Muhetaer, L. Dong, Y. Wang, Y. Ma, H. Du, *J. Am. Ceram. Soc.* **2024**, *107*, 8224, https://doi.org/10.1111/jace.20049.
[44] D. Liu, X. Fan, S. Jiang, R. Tao, Z. Chu, Y. Li, *J. Colloid Interface Sci.* **2025**, *696*, 137893, https://doi.org/10.1016/j.jcis.2025.137893.

[45] T. N. Jahangir, T. A. Kandiel, N. Mahar, A. Z. Khan, A. A. Al-Saadi, *Mater Today Energy.* **2024**, *40*, 101469, https://doi.org/10.1016/j.mtener.2023.101469.

[46] A. K. Salih, A. Z. Khan, Q. Drmosh, T. Kandiel, M. Qamar, T. Jahangir, C. Ton-That, Z. Yamani, *ACS Appl. Nano Mater.* **2024**, *7*, 14115, https://doi.org/10.1021/acsanm.4c01527.

[47] S. Chen, Y. Nagai, Z. Pan, K. Katayama, *ACS Appl. Mater. Interfaces* **2024**, *16*, 33611, https://doi.org/10.1021/acsami.4c06220.

[48] Y. H. Kim, Y. G. Bae, W. Y. Soh, *ChemPhysChem* **2024**, *25*, 202300894, https://doi.org/10.1002/cphc.202300894.

[49] X. Zhang, X. Wang, D. Wang, J. Ye, *ACS Appl. Mater. Interfaces* **2019**, *11*, 5623, https://doi.org/10.1021/acsami.8b05477.

[50] G. Ai, R. Mo, H. Li, J. Zhong, *Nanoscale* **2015**, *7*, 6722, https://doi.org/10.1039/C5NR00863H.

[51] N. S. Powar, S. Kim, J. Lee, E. Gong, C. B. Hiragond, D. Kim, T. Zhang, M. Kim, S.-I. In, *Appl. Catal. B: Environ.* **2024**, *352*, 124006, https://doi.org/10.1016/j.apcatb.2024.124006.

[52] F. J. Willars-Rodríguez, M. A. Hernández-Landaverde, A. Zavala-Franc, E. A. Chávez-Urbiola, P. Vorobiev, Y. V. Vorobiev, *Mater. Chem. Phys.* **2024**, *312*, 128636, https://doi.org/10.1016/j.matchemphys.2023.128636.

[53] X. Gao, X. Li, Z. Zhu, Y. Gao, Q. Wang, F. Zhu, Z. Xie, *Sci. Rep.* **2017**, *7*, 973, https://doi.org/10.1038/s41598-017-01124-5.

[54] G. Yang, B. Yang, T. Xiao, Z. Yan, *Appl. Surf. Sci.* **2013**, *283*, 402, https://doi.org/10.1016/j.apsusc.2013.06.122.

[55] C. Feng, L. Zhang, Z. Cheng, *ChemistrySelect* **2020**, *5*, 2142, https://doi.org/10.1002/slct.201904603.

[56] Y. Wang, L. Zhao, X. Cai, Y. Chen, J. Xu, L. Zhang, L. Lin, X. Dai, Y. Jiang, J. Liao, Y. Zhang, *Environ. Sci. Pollut. Res.* **2024**, *31*, 15091, https://doi.org/10.1007/s11356-024-32190-8.

[57] X. Han, C. Zhao, Z. Pan, X. Tang, Z. Jiang, *Smart Mater. Med.* **2022**, *3*, 168, https://doi.org/10.1016/j.smaim.2022.01.002.

[58] M. Zubair, I. H. Svenum, M. Rønning, J. Yang, *Catalyst* **2020**, *10*, 358, https://doi.org/10.3390/catal10040358.

[59] J. C. Yu, J. Yu, H. Y. Tang, L. Zhang, *J. Mater. Chem.* **2002**, *12*, 81, https://doi.org/10.1039/B102909F.

[60] F. Orlando, L. Artiglia, H. Yang, X. Kong, K. Roy, A. Waldner, S. Chen, T. Bartels-Rausch, M. Ammann, *J. Phys. Chem. Lett.* **2019**, *10*, 7433, https://doi.org/10.1021/acs.jpclett.9b02779.

[61] D. Cabrera-German, M. Martínez-GilLorenzo, L. Fuentes-RíosZeuz, Z. Montiel-González, D. A. Mazón-Montijo, M. Sotelo-Lerma, *ACS Omega* **2023**, *8*, 48056, https://doi.org/10.1021/acsomega.3c06848.

[62] L. Feng, L. Zhang, X. Chen, C. Zhang, G. Mao, H. Wang, *Chem. Eng. J.* **2022**, *441*, 136073, https://doi.org/10.1016/j.cej.2022.136073.

[63] C. Fan, X. Wang, H. Sang, F. Wang, *Int. J. Photoenergy* **2012**, *2012*, 492746, https://doi.org/10.1155/2012/492746.

[64] J. Tian, L. Lv, C. Fei, Y. Wang, X. Liu, G. Cao, *J. Mater. Chem. A* **2014**, *2*, 19653, https://doi.org/10.1039/C4TA04534C.

[65] Y. Y. Song, K. S. Park, K. H. Park, S. K. Oh, S. C. Yu, H. J. Kang, K. W. Lee, *J. Korean Phys. Soc.* **2008**, *52*, 106, https://doi.org/10.3938/jkps.52.106.

[66] V. N. Nguyen, M. T. Doan, M. V. Nguyen, *J. Mater. Sci.: Mater. Electron.* **2019**, *30*, 926, https://doi.org/10.1007/s10854-018-0363-8.

[67] M. Huang, M. Yu, R. Si, X. Zhao, S. Chen, K. Liu, X. Pan, *Catalysts* **2023**, *13*, 1123, https://doi.org/10.3390/catal13071123.

[68] D. K. Zhong, S. Choi, D. R. Gamelin, *J. Am. Chem. Soc.* **2011**, *133*, 18370, https://doi.org/10.1021/ja207348x.

[69] Z. Song, X. Zhu, Y. Zheng, A. Wang, S. Li, Y. Fan, M. Cai, M. Cheng, Y. Wei, S. Sun, *Catal. Lett.* **2020**, *150*, 1878, https://doi.org/10.1007/s10562-019-03084-z.

[70] M. P. Valkonen, T. Kanniainen, S. Lindroos, M. Leskela, E. Rauhala, *Appl. Surf. Sci.* **1997**, *115*, 386, https://doi.org/10.1016/S0169-4332(97)00008-1.

[71] T. R. Nivedhitha, H. Bajpai, J. V. Oommen, A. Abraham, I. Chauhan, C. S. Gopinath, *ACS Sus. Chem. Eng.* **2024**, *12*, 14841, https://doi.org/10.1021/acssuschemeng.4c05853.

[72] T. She, J. Tian, L. Lv, C. Fei, Y. Wang, T. Pullerits, G. Cao, *Electrochim. Acta* **2016**, *191*, 62, https://doi.org/10.1016/j.electacta.2016.01.056.

[73] W. MacSwain, H. Lin, Z.-J. Li, S. Li, C. Chu, L. Dube, O. Chen, G. Leem, W. Zheng, *J. Mater. Chem. A* **2023**, *11*, 7066, https://doi.org/10.1039/D2TA08409K.

[74] Z.-J. Li, S. Li, A. H. Davis, E. Hofman, G. Leem, W. Zheng, *Nano Res.* **2020**, *13*, 1668, https://doi.org/10.1007/s12274-020-2790-0.

[75] P. Y. Naidu, M. Kumar, B. Meena, S. Challapalli, *Int. J. Hydrog. Energy* **2025**, *166*, 151000, https://doi.org/10.1016/j.ijhydene.2025.151000.